

Letter

Encapsulation of molybdenum carbide nanoclusters inside zeolite micropores enables synergistic bifunctional catalysis for anisole hydrodeoxygenation

Takayuki Iida, Manish Shetty, Karthick Murugappan, Zhenshu Wang, Koji Ohara, Toru Wakihara, and Yuriy Roman-Leshkov

ACS Catal., **Just Accepted Manuscript** • DOI: 10.1021/acscatal.7b03175 • Publication Date (Web): 20 Oct 2017Downloaded from <http://pubs.acs.org> on October 20, 2017**Just Accepted**

“Just Accepted” manuscripts have been peer-reviewed and accepted for publication. They are posted online prior to technical editing, formatting for publication and author proofing. The American Chemical Society provides “Just Accepted” as a free service to the research community to expedite the dissemination of scientific material as soon as possible after acceptance. “Just Accepted” manuscripts appear in full in PDF format accompanied by an HTML abstract. “Just Accepted” manuscripts have been fully peer reviewed, but should not be considered the official version of record. They are accessible to all readers and citable by the Digital Object Identifier (DOI®). “Just Accepted” is an optional service offered to authors. Therefore, the “Just Accepted” Web site may not include all articles that will be published in the journal. After a manuscript is technically edited and formatted, it will be removed from the “Just Accepted” Web site and published as an ASAP article. Note that technical editing may introduce minor changes to the manuscript text and/or graphics which could affect content, and all legal disclaimers and ethical guidelines that apply to the journal pertain. ACS cannot be held responsible for errors or consequences arising from the use of information contained in these “Just Accepted” manuscripts.



Encapsulation of Molybdenum Carbide Nanoclusters inside Zeolite Micropores Enables Synergistic Bifunctional Catalysis for Anisole Hydrodeoxygenation

Takayuki Iida^{1,2}, Manish Shetty², Karthick Murugappan², Zhenshu Wang², Koji Ohara³, Toru Wakihara^{1*}, and Yuriy Román-Leshkov^{2*}

1) Department of Chemical System Engineering, The University of Tokyo, 7-3-1 Hongo, Bunkyo-ku, Tokyo 113-8656, Japan

2) Department of Chemical Engineering, Massachusetts Institute of Technology, 25 Ames Street, Cambridge, Massachusetts 02139, United States of America

3) Japan Synchrotron Radiation Research Institute/SPring-8, Kouto 1-1-1, Sayo-gun, Hyogo 679-5198, Japan

ABSTRACT: Molybdenum carbide (MoC_x) nanoclusters were encapsulated inside the micropores of aluminosilicate FAU zeolites to generate highly active and selective bifunctional catalyst for the hydrodeoxygenation of anisole. Interatomic correlations obtained with differential pair distribution function analysis confirmed the intraparticle structure and the uniform size of the MoC_x nanoclusters. The reactivity data showed the preferential production of alkylated aromatics (such as toluene and xylene) over benzene during the hydrodeoxygenation of anisole as well as the minimization of unwanted CH₄ formation. Control experiments demonstrated the importance of MoC_x encapsulation to generate an efficient bifunctional catalyst with superior carbon utilization and on-stream stability.

Keywords: *Hydrodeoxygenation, bifunctional catalyst, zeolite, carbide, pair distribution function*

Bifunctional catalysts have been reported to open up remarkable reaction routes to desired products at high yields in multi-step reactions¹. Metal supported zeolites are promising materials for acid/metal bifunctional catalysis, as exemplified in the simultaneous Fischer-Tropsch/hydrocracking², as well as in the hydroisomerization of alkanes³ using cobalt² and platinum³ metals supported on zeolites, respectively. The efficient combination of zeolite pore confinement effects with nanoparticles having unconventional redox-active sites, such as transition metal carbides, will provide further possibilities for developing new bifunctional catalysts. For some reactions, early transition metal carbides have shown similar catalytic activity to that of group VIII noble metals⁴, and are gaining more attention in applications such as electrocatalysis^{5,6}, hydrodeoxygenation^{7,8} and Fischer-Tropsch chemistry^{9,10}. Indeed, various transition metal carbides supported on ZSM-5 zeolites are the preferred catalysts for methane dehydroaromatization¹¹⁻¹³.

The efficient bifunctionality of these materials hinges on the molecular proximity of the metallic sites of the nanoparticles with the Brønsted acid sites of the zeolites^{2,13}. Therefore, the controlled synthesis and detailed characterization of the encapsulated metallic species (usually < 1 nm in diameter) is of critical importance to direct targeted reaction pathways. A major bottleneck for achieving these goals lies in the lack of methodologies for understanding the structural nature of the metallic nanoclusters, such as the particle size distribution and atomic-scale intraparticle

structure. The limited loadings (usually ~1 wt%) and the small particle sizes prevent the use of conventional analytical techniques such as powder X-ray diffraction (PXRD)¹⁴. Similarly, while transmission electron microscopy (TEM) can provide information regarding the particle size and morphology, other structural information is limited. Extended X-ray absorption fine structure (EXAFS)¹⁵ and chemisorption¹⁶ are powerful tools in characterizing nanoclusters composed of single metallic element, providing information regarding crystal structure and particle size, but the accurate interpretation of these measurements becomes more challenging for heterometallic nanoparticles. For example, CO chemisorption values on a carbide are highly dependent on synthesis conditions and the nature of the surface (e.g., mild passivation or presence of coke)^{17,18}, and thereby, dispersion measurements may provide inaccurate results. The development of reliable characterization tools for carbide nanoclusters is critical for the design and implementation of these materials in various catalytic processes.

In this work, we first encapsulated molybdenum carbide (MoC_x) nanoclusters within the pores of zeolites with the faujasite (FAU) topology and then used pair distribution function (PDF) analysis to conduct a detailed characterization of their structures. While the formation of MoC_x species inside the zeolites pores has been demonstrated in prior studies¹¹⁻¹³, their particle size distribution and intraparticle atomic arrangement have remained ambiguous¹⁹. PDF represents the probability of finding an interatomic

distance inside an unit volume, and has conventionally been used to describe disordered structures that are not amenable to conventional diffraction techniques (e.g., amorphous vitreous glasses)²⁰. The availability of this method for describing structural arrangements at distances beyond those reliably quantifiable by EXAFS (>5 Å) has allowed the acquisition of information on other crystalline nanostructures including heterometallic nanoparticles^{21,22} and even disorders in bulk crystals²³. We investigated the encapsulated MoC_x nanoclusters as catalysts for the vapor phase hydrodeoxygenation (HDO) of anisole, a biomass-based model compound with methoxy benzene motif prevalent in lignin's structure^{24,25}. The use of pristine molybdenum carbide (Mo₂C) catalysts for this reactions has been shown to produce benzene and methane as the main products with high selectivity and minimal formation of ring-saturated byproducts²⁵. Zeolites are known to be effective deoxygenation agents for pyrolysis oil, at the expense of producing large amounts of coke²⁶. We show that the bifunctional MoC_x/FAU catalyst displayed stable (trans)alkylation and hydrodeoxygenation activity, generating a high proportion of alkylated aromatics (alkylated aromatics/benzene ratio ~2.9 C-mol%), while minimizing the formation of undesirable products, namely methane, due to close interaction between strong zeolitic Brønsted acid sites and carbidic metallic sites (Figure 1).

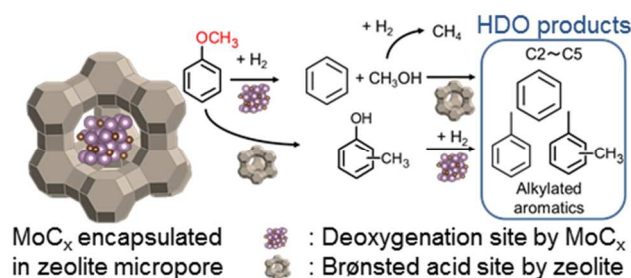


Figure 1. Bifunctional anisole conversion by MoC_x encapsulated FAU zeolite catalyst for producing alkylated aromatics and C₂~C₅ light gas elements by the combination of zeolitic Brønsted acid sites and MoC_x deoxygenation sites.

The MoC_x/FAU catalysts were synthesized by solid state ion exchange of Mo⁶⁺ with (NH₄)₆Mo₇O₂₄·4H₂O followed by a carburization treatment under CH₄ and H₂ flow at 973 K. The Si/Al ratio of the zeolite was 15, and the Mo/Al ratio was fixed to 0.5, resulting in a Mo loading of 5 wt%. Pristine Mo₂C was prepared by carburization of (NH₄)₆Mo₇O₂₄·4H₂O at 923K for 3 h. Detailed catalyst preparation procedures are summarized in the Supporting Information.

As expected, conventional PXRD patterns associated with Mo₂C were not detected in the MoC_x/FAU samples (Figure S1). Therefore, structural characterization of MoC_x species was performed using differential pair distribution function (d-PDF)^{22,27}, an applied form of PDF analysis useful for determining specific phases in binary mixtures. This technique involves taking the difference between the pair distribution functions, $G(r)$, of the mixture and the admixed secondary phase as shown in Eqs (1) and (1)' below:

$$G_{A+B}(r) \cong x_A G_A(r) + x_B G_B(r) \dots (1)$$

$$x_A G_A(r) \cong G_{A+B}(r) - x_B G_B(r) \dots (1)'$$

where A and B represent specific phases (in this case A represents the MoC_x phase and B represents the FAU zeolite phase, A + B represents the mixture of the two phases, and x_A and x_B are coefficients). The calculated d-PDF result for MoC_x/FAU is shown in Figure 2 A, and that for the physical mixture of Mo₂C and FAU zeolite with equivalent Mo weight loading is shown in Figure 2 B. To account for the correlation peaks, the theoretical $G(r)$ of Mo₂C (hcp phase) was calculated using PDFgui software²⁸, and is shown in Figure 2 C for comparison. Ziman-Faber total structure factors, $S(Q)$, used for the calculation of the PDFs are summarized in Figure S2. Correlations corresponding to the Mo₂C phase were observed up to $r \sim 7$ Å for MoC_x/FAU (shown with black dotted lines), but were not observed at longer distances (shown with red dotted lines) showing that the nanoclusters only possess structural ordering up to around 7 Å, corresponding no larger than three unit cells. On the contrary, the d-PDF of the physical mixture possessed correlation ranging beyond this distance, confirming that if a bulk structure had formed, all the theoretical correlations in this distance range should be apparent. Thus, these data are in agreement with the presence of ~10 Å sized nanoclusters as observed in the TEM images shown in Figure 2 D. Assignment of the correlation peaks in Mo₂C were made using the PDFgui software²⁸, and most correlations visible were found to originate from Mo-C correlations (at 2.0 Å) or Mo-Mo (other correlations shown with dotted lines) due to the relatively large X-ray scattering factor by Mo compared to C (Figure S3). Further, correlations corresponding to hcp Mo₂C phase were confirmed in the d-PDF of the physical mixture wherein standalone bulk Mo₂C species are present outside of the zeolite crystal.

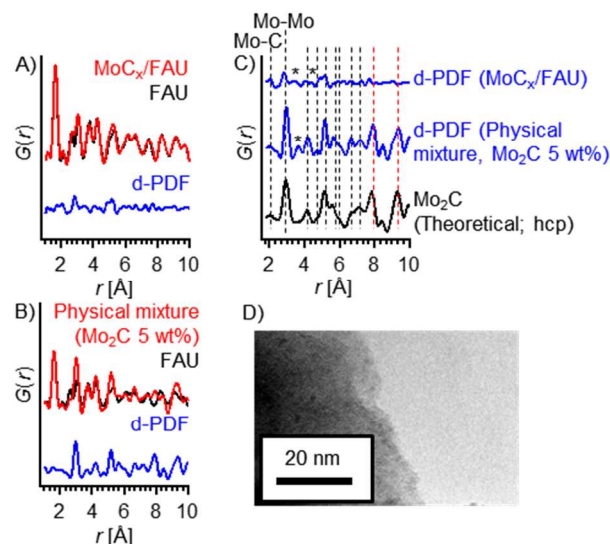


Figure 2. A) Pair distribution function, $G(r)$, of MoC_x/FAU, parent FAU and calculated d-PDF of occluded MoC_x element, B) Pair distribution function, $G(r)$, of a physical mixture of Mo₂C and FAU (5 wt% Mo), parent FAU and calculated d-PDF of Mo₂C element, C) Comparison of d-PDF results with the simulated pair distribution function, $G(r)$, of Mo₂C (hcp phase)

using PDFgui software²⁸, and D) Typical TEM image of MoC_x/FAU. Correlations corresponding to Mo₂C are shown with dotted lines, and the correlations assigned to MoO_x species are marked with an asterisk(*).

The PDF analysis of the MoC_x/FAU material showed correlations that did not belong to the Mo₂C phase at $r = 3.3$ and 4.4 Å (shown with asterisks(*)). A comparison with various control materials including bcc Mo(0), MoO₂, and MoO₃ (Figure S4) confirms that the observed peaks match those of MoO_x species, which are likely located on the surface of the carbide as a passivation layer. The absence of correlation peaks at $r = 2.7$ and 3.2 Å corresponding to Mo(0) (bcc) denotes that any metallic molybdenum species present in the sample are below the detection limit. These data are in agreement with X-ray photoelectron spectroscopy (XPS) data probing molybdenum oxidation states of surface passivated MoC_x/FAU at Mo 3d band, in which similar amounts of Mo²⁺ species was observed with the bulk surface-passivated Mo₂C sample (Figure S5). A PDF comparison with the orthorhombic Mo₂C and α -MoC_{1-x} phases showed that distinguishing the hcp phase with the orthorhombic Mo₂C phase is difficult through PDF analysis due to the high similarity in the peak positions of the two phases (also the case with PXRD⁸), whereas the presence of α -MoC_{1-x} phase can be tentatively ruled out by comparing the number of peaks between $r = 5.8 \sim 6.2$ Å (Figure S6). Since it is difficult to unambiguously assign the stoichiometry of the nanocluster and since it is not possible to assign a crystal structure to a solid that does not possess diffraction patterns, the term MoC_x is used herein to describe these moieties. The N₂ physisorption data revealed the decrease in micropore volume from 0.24 (FAU) to 0.21 cc g⁻¹ (MoC_x/FAU), showing the encapsulation of the MoC_x nanoclusters in the zeolite micropores (Figure S7, and Table S3). Taken together, our data imply that phase-pure MoC_x nanoclusters of ~ 1 nm in size were effectively encapsulated within the pores of FAU. Clearly, the capability of PDF analyses to extract the structural information up to 10 Å is essential for describing the architecture of the encapsulated MoC_x nanoclusters. To the best of our knowledge, this represents the first example of a pair distribution function analysis applied for the structural characterization of transition metal carbide nanoclusters.

MoC_x/FAU was used for the coupled HDO and alkylation of anisole with the aim to obtain a higher selectivity to alkylated aromatic groups (i.e. toluene, xylene etc.) in place of the benzene/methane mixture traditionally obtained with bulk Mo₂C catalysts. The reaction was performed at 523 K, with $p_{\text{Total}} = 1.013$ bar, $p_{\text{anisole}} = 0.0079$ bar and balance H₂, under the absence of external and internal diffusion limitations (detailed experimental conditions are summarized in the SI). The product distribution consisted of benzene, toluene, alkylated aromatics C₈₊ (i.e. ethylbenzene, xylenes and other deoxygenated aromatics with more than eight carbons), phenol, alkylated phenols (phenolic compounds with more than seven carbon atoms such as cresols), alkylated anisoles (i.e. methyl anisole), and light gas C₅- (aliphatic hydrocarbons with carbon numbers between one and five such as methane and ethane). To understand the role of carbide encapsulation and its syn-

ergy with acid sites, control reactions were also performed using a pristine Mo₂C, a parent FAU zeolite, and a physical mixture of Mo₂C and FAU zeolite with identical metal and/or Brønsted acid site loadings (designated as Mo₂C+FAU; site count was performed by CO chemisorption and NH₃-TPD, respectively, and the results are summarized in Table S4). To assess the effectiveness of MoC_x/FAU catalysts on the formation of alkylated aromatics in comparison to benzene, the alkylation ratio was defined as follows:

$$\text{Alkylation ratio} = \frac{\sum \text{Produced alkylated aromatics [C - mol\%]}}{\text{Produced benzene [C - mol\%]}}$$

All the catalysts used were carburized in-situ at 973 K under a CH₄/H₂ atmosphere before the reaction to avoid the formation of an oxide passivation layer prior to the introduction of the feed.

For all the catalysts, the conversion (Figure 3) and the product selectivity values (Figure S8-S11) reached steady state after ca. 1000 min on stream. Note that under identical reaction conditions and similar number of active sites, the MoC_x/FAU catalyst maintained high conversions, typically above $\sim 97\%$, whereas the conversion of Mo₂C+FAU settled around $\sim 61\%$ after 1200 min of reaction after reaching steady state, thereby displaying apparent higher reactivity and stability by encapsulation.

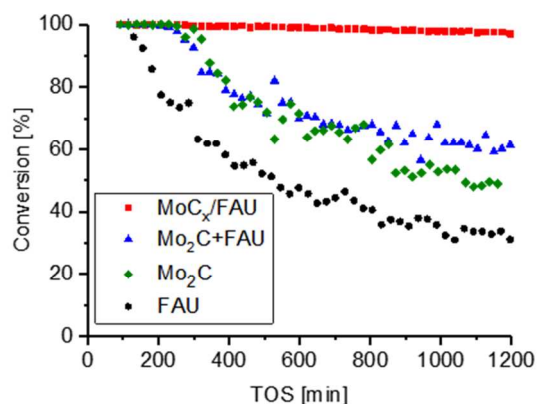


Figure 3. Conversion time profile of anisole over MoC_x/FAU, pristine Mo₂C, parent FAU, and Mo₂C+FAU catalysts. All catalysts possess same metal and/or Brønsted acid site loadings. Reaction conditions: Reaction temperature: 523 K, Anisole feed: 150 μ l/h, Catalyst loading: 750 mg for MoC_x/FAU, 322 mg for Mo₂C, 600 mg for parent FAU, 922 mg for Mo₂C+FAU, $p_{\text{Total}} = 1.013$ bar, $p_{\text{anisole}} = 0.0079$ bar, and balance H₂.

The product distribution was significantly different across all samples (Figure 4). For MoC_x/FAU, a significant amount of alkylated aromatics was observed, with an alkylation ratio of 2.9 based on a yield of 17 C-mol% for alkylated products vs 5.8 C-mol% for benzene. This value was maintained throughout the duration of the experiment. In contrast, the experiment using the FAU zeolite generated exclusively phenols and alkylated anisoles, both of which are products formed by (trans)alkylation reaction catalyzed by the Brønsted acid sites of the zeolites, thus

showing the lack of HDO reactivity by parent zeolite catalyst. This observation confirms that MoC_x species are responsible for the HDO reactivity. Bifunctional catalysis by different materials has been performed for anisole HDO reactions^{29–33}, with maximum alkylation ratios only ~1.8 (MoO₃/ZrO₂)³³. Evidently, the MoC_x/FAU catalyst is a highly effective bifunctional catalyst with enhanced HDO/alkylation performance over current state of the art catalysts for anisole upgrading. While the Mo₂C+FAU mixture also formed alkylated aromatics as products, the alkylation ratio only reached a value of 0.47, which is on par with other bifunctional catalysts^{29–33}. The product selectivity to alkylated anisoles was significantly higher for Mo₂C+FAU (20 C-mol%) than for MoC_x/FAU (0.3 C-mol%). The formation of alkylated aromatics can clearly be attributed to the transalkylation of methoxy groups from one anisole molecule to another by the Brønsted acid sites. The prompt deoxygenation of the alkylated anisole species is enabled by the molybdenum carbide species in close vicinity of the Brønsted acid sites for MoC_x/FAU, whereas this is not the case for Mo₂C+FAU, which has a significantly longer physical distance between the two sites, allowing the desorption of these intermediate species before the subsequent deoxygenation step. It should be noted that the binding energy of C-O bond in anisole was reported to be lower in comparison to that of C-O bond in phenol³¹, and we hypothesize that this difference is likely the key factor for the selective deoxygenation of the (alkylated) anisole intermediate species by MoC_x/FAU compared to phenols.

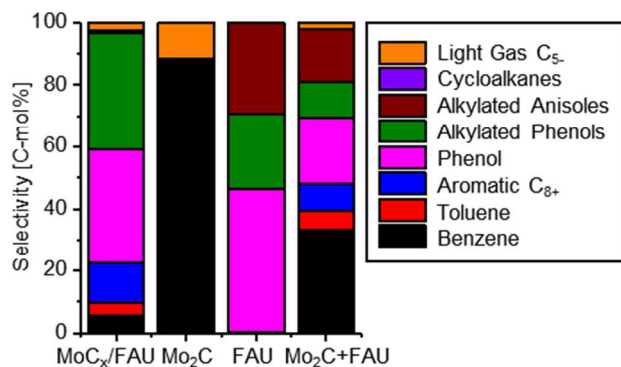


Figure 4. Reaction selectivity of MoC_x/FAU, pristine Mo₂C, parent FAU, and Mo₂C+FAU catalysts at the final point of reaction run (TOS = 1200 min). The conversions of these catalysts were 97% (MoC_x/FAU), 49% (Mo₂C), 31% (FAU), and 61% (Mo₂C+FAU). Reaction conditions are identical to those described in Figure 2. Aromatics C₈₊ include ethylbenzene, xylenes and the other deoxygenated aromatics having more than eight carbons. Alkylated phenols include phenolic compounds with more than seven carbon atoms such as cresols. Alkylated anisoles include substituted anisoles with more than eight carbon atoms such as methyl anisole. Light gas C₅ includes aliphatic hydrocarbons with carbon numbers between one and five such as methane and ethane.

Remarkably, when using the bifunctional MoC_x/FAU materials, methane formation was severely hindered (0.2 C-mol% in selectivity), while C₂~C₅ hydrocarbons (~2.6 C-mol% selectivity in total) was confirmed inside the light

gas C₅- fraction (Figure 5 A)). This result is in stark contrast to bulk Mo₂C catalysts, which showed selectivity values of 12 C-mol% to methane²⁵. The reaction pathway to generate C₂~C₅ light gas elements was investigated by monitoring the aliphatic carbon/benzene ring molar ratio throughout the reaction. We note that since the aim of the calculation was to elucidate the origin of C₂~C₅ elements, cyclohexanes were lumped in into the aromatics portion because they are produced by the hydrogenation of the aromatic rings. As seen in Figure 5 B, the aliphatic carbon/benzene ring molar ratio was approximately 1 throughout the entire reaction, thereby suggesting that the C₂~C₅ light gas elements were not produced from hydrogenation/hydrocracking. Instead, C₂~C₅ light gases are likely formed from C-C coupling reactions of anisole-derived methanol intermediates via methanol-to-olefin pathways at the zeolite acid sites.

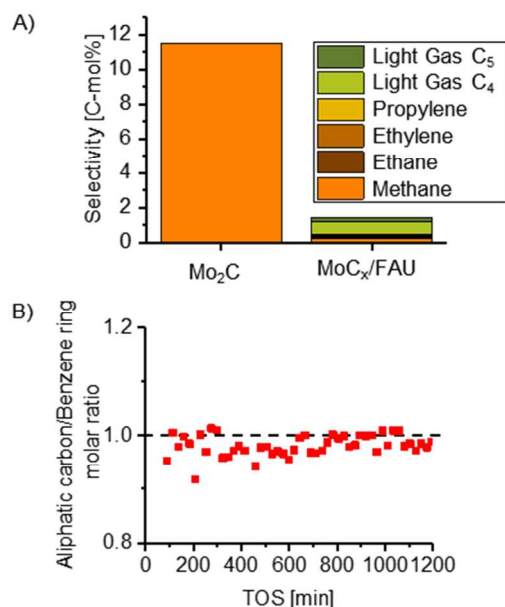


Figure 5. A) Final product selectivity (TOS = 1200 min) among the light gas C₅- products (Conversion = 97% for MoC_x/FAU; Conversion = 49% for Mo₂C), and B) Calculated results for aliphatic carbon/benzene ring molar balance throughout the reaction run for MoC_x/FAU. Reaction conditions identical to those described in Figure 3.

The fate of methoxy groups during the reaction with MoC_x/FAU catalysts should result in two distinct reaction routes, namely: 1) hydrodeoxygenation (benzene ring-oxygen bonding cleavage) by MoC_x nanoclusters followed by alkylation of the intermediate methanol groups to the aromatics; and 2) transalkylation of methoxy group to the aromatics followed by the deoxygenation of the phenolic hydroxy group. To realize such tandem reaction mechanism, the presence of both selective deoxygenation sites by molybdenum carbide nanoclusters, as well as the strong Brønsted acidity of zeolites are required.

Nanocluster agglomeration in MoC_x/FAU during the reaction was ruled out from TEM images showing similar particle sizes as those observed before reaction (Figure S12). Also, the deactivation of MoC_x/FAU was investigated

with an experiment using a reduced catalyst loading (1/3 of the original loading) to operate at conversion values under 100% (Figure S13). At these conditions, this catalyst featured two deactivation profiles: one during the transient period (TOS < 400 min), followed by a more gradual one thereafter. Notably, the catalyst was fully regenerated by a hydrogen treatment at 500°C for 4 h, thus confirming that catalyst deactivation was reversible and also ruling out nanocluster sintering. TGA measurements revealed the presence of 8.6 wt% of carbon deposits relative to the catalyst mass, pointing at coking as a possible deactivation mode. Although XPS does not show that bulk oxidation of the MoC_x nanoclusters occurred even after exposure to air, we cannot rule out the formation of an oxycarbide layer during reaction.

In summary, d-PDF analyses confirmed that MoC_x/FAU catalysts comprising molybdenum carbide nanoclusters with ~1 nm diameter were successfully encapsulated within the pores of FAU zeolite with high uniformity. This material was shown to be an efficient catalyst for the production of alkylated aromatics (alkylation ratio: 2.9) from anisole, while preventing the formation of methane byproducts (0.2 C-mol%) in comparison to the pristine Mo₂C catalyst (12 C-mol%). From the control experiments, the close proximity of the Brønsted acid sites around the metallic sites was suggested to be the key factor for enabling such reaction selectivity values and for increasing on-stream stability. The current findings not only suggest the existence of important advantages from having transition metal carbide nanoclusters inside zeolite structure for catalytic applications in HDO processes, but also open up new avenues for other chemical reactions that can make good use of bifunctionality of the metallic sites and zeolitic Brønsted acid sites.

ASSOCIATED CONTENT

Supporting Information. PXRD patterns, further d-PDF analysis results, XPS spectra, BET specific surface areas, micropore volumes, Ziman-Faber total structure factor, $S(Q)$, used for calculating the pair distribution functions, $G(r)$, selectivity time profile of various catalysts, evaluation of external and internal mass transfer, TEM image of catalyst after reaction. This material is available free of charge on the Internet at <http://pubs.acs.org>.

AUTHOR INFORMATION

Corresponding Author

*wakahara@chemsys.t.u-tokyo.ac.jp

*yroman@mit.edu

Present Addresses

†If an author's address is different than the one given in the affiliation line, this information may be included here.

Author Contributions

The manuscript was written through contributions of all authors.

ACKNOWLEDGMENT

The High Energy Total X-ray Scattering experiments conducted at SPring-8 were approved by the Japan Synchrotron Radiation Research Institute (Proposal Nos. 2015B0115 and 2016A0115). T. I. thanks the Japan Society for the Promotion of Science for a Grant-in-aid for Scientific research, and the Program for Leading Graduate Schools, "Global Leader Program for Social Design and Management (GSDM)", by the Ministry of Education, Culture, Sports, Science and Technology, for the financial support. This work was supported by the U.S. Department of Energy, Office of Basic Energy Sciences under Award No. DE-SC0016214.

REFERENCES

- Jiao, F.; Li, J. J.; Pan, X. L.; Xiao, J. P.; Li, H. B.; Ma, H.; Wei, M. M.; Pan, Y.; Zhou, Z. Y.; Li, M. R.; Miao, S.; Li, J.; Zhu, Y. F.; Xiao, D.; He, T.; Yang, J. H.; Qi, F.; Fu, Q.; Bao, X. H. *Science* **2016**, *351*, 1065–1068.
- Sartipi, S.; Makkee, M.; Kapteijn, F.; Gascon, J. *Catal. Sci. Technol.* **2014**, *4*, 893–907.
- Guisnet, M. *Catal. Today* **2013**, *218–219*, 123–134.
- Levy, R. B.; Boudart, M. *Science* **1973**, *181*, 547–549.
- Esposito, D. V.; Hunt, S. T.; Kimmel, Y. C.; Chen, J. G. G. *J. Am. Chem. Soc.* **2012**, *134*, 3025–3033.
- Hunt, S. T.; Milina, M.; Alba-Rubio, A. C.; Hendon, C. H.; Dumesic, J. A.; Roman-Leshkov, Y. *Science* **2016**, *352*, 974–978.
- Xiong, K.; Yu, W.; Vlachos, D. G.; Chen, J. G. *ChemCatChem* **2015**, *7*, 1402–1421.
- Sullivan, M. M.; Chen, C. J.; Bhan, A. *Catal. Sci. Technol.* **2016**, *6*, 602–616.
- Santos, V. P.; Wezendonk, T. A.; Jaen, J. J. D.; Dugulan, A. I.; Nasalevich, M. A.; Islam, H. U.; Chojecki, A.; Sartipi, S.; Sun, X.; Hakeem, A. A.; Koeken, A. C. J.; Ruitenbeek, M.; Davidian, T.; Meima, G. R.; Sankar, G.; Kapteijn, F.; Makkee, M.; Gascon, J. *Nat. Commun.* **2015**, *6*, 6451.
- Zhong, L. S.; Yu, F.; An, Y. L.; Zhao, Y. H.; Sun, Y. H.; Li, Z. J.; Lin, T. J.; Lin, Y. J.; Qi, X. Z.; Dai, Y. Y.; Gu, L.; Hu, J. S.; Jin, S. F.; Shen, Q.; Wang, H. *Nature* **2016**, *538*, 84–87.
- Borry, R. W.; Kim, Y. H.; Huffsmith, A.; Reimer, J. A.; Iglesia, E. *J. Phys. Chem. B* **1999**, *103*, 5787–5796.
- Li, W.; Meitzner, G. D.; Borry, R. W.; Iglesia, E. *J. Catal.* **2000**, *191*, 373–383.
- Kosinov, N.; Coumans, F. J. A. G.; Uslamin, E. A.; Wijkema, A. S. G.; Mezari, B.; Hensen, E. J. M. *ACS Catal.* **2017**, *7*, 520–529.
- Farrusseng, D.; Tuel, A. *New J. Chem.* **2016**, *40*, 3933–3949.
- Alexeev, O.; Gates, B. C. *Top. Catal.* **2000**, *10*, 273–293.
- Hammer, B.; Morikawa, Y.; Norskov, J. K. *Phys. Rev. Lett.* **1996**, *76*, 2141–2144.
- Lee, W.; Kumar, A.; Wang, Z.; Bhan, A. *ACS Catal.* **2015**, *5*, 4104–4114.
- Oyama, S. T. *Catal. Today* **1992**, *15*, 179–200.
- Gao, J.; Zheng, Y.; Fitzgerald, G. B.; de Joannis, J.; Tang, Y.; Wachs, I. E.; Podkolzin, S. G. *J. Phys. Chem. C* **2014**, *118*, 4670–4679.
- Proffen, T.; Billinge, S. J. L.; Egami, T.; Louca, D. *Zeitschrift für Krist.* **2003**, *218*, 132–143.
- Billinge, S. J.; Kanatzidis, M. G. *Chem. Commun.* **2004**, 749–760.
- Chupas, P. J.; Chapman, K. W.; Chen, H. L.; Grey, C. P. *Catal. Today* **2009**, *145*, 213–219.
- Petkov, V.; Jeong, I.-K.; Chung, J. S.; Thorpe, M. F.; Kycia, S.; Billinge, S. J. L. *Phys. Rev. Lett.* **1999**, *83*, 4089–4092.
- Zakzeski, J.; Bruijninx, P. C. A.; Jongerius, A. L.; Weckhuysen, B. M. *Chem. Rev.* **2010**, *110*, 3552–3599.
- Lee, W. S.; Wang, Z.; Wu, R. J.; Bhan, A. *J. Catal.* **2014**, *319*, 44–53.

1 (26) Jae, J.; Tompsett, G. A.; Foster, A. J.; Hammond, K. D.; Au-
2 erbach, S. M.; Lobo, R. F.; Huber, G. W. *J. Catal.* **2011**, *279*, 257–
3 268.

4 (27) Chapman, K. W.; Chupas, P. J.; Kepert, C. J. *J. Am. Chem.*
5 *Soc.* **2005**, *127*, 11232–11233.

6 (28) Farrow, C. L.; Juhas, P.; Liu, J. W.; Bryndin, D.; Božin, E.
7 S.; Bloch, J.; Proffen, T.; Billinge, S. J. L. *J. Phys. Condens. Matter*
8 **2007**, *19*, 335219.

9 (29) Zhu, X. L.; Lobban, L. L.; Mallinson, R. G.; Resasco, D. E. *J.*
10 *Catal.* **2011**, *281*, 21–29.

(30) Foo, G. S.; Rogers, A. K.; Yung, M. M.; Sievers, C. *ACS*
Catal. **2016**, *6*, 1292–1307.

(31) Prasomsri, T.; Shetty, M.; Murugappan, K.; Román-
Leshkov, Y. *Energy Environ. Sci.* **2014**, *7*, 2660–2669.

(32) Anderson, E.; Crisci, A.; Murugappan, K.; Roman-
Leshkov, Y. *ChemSusChem* **2017**, *10*, 2226–2234.

(33) Shetty, M.; Murugappan, K.; Green, W. H.; Roman-
Leshkov, Y. *ACS Sustain. Chem. Eng.* **2017**, *5*, 5293–5301.

Insert Table of Contents artwork here

